Contrasting impacts of irrigation and deforestation on Lancang-Mekong River Basin hydrology

Check for updates

Hao Huang[1], Junguo Liu [1,2] ✉, Luca Guillaumot [3], Aifang Chen[4], Inge E. M. de Graaf [5] & Deliang Chen [6,7]

Irrigation expansion and subsequent deforestation substantially affect large basin variability. However, given the complex interactions between hydrological variables, a more comprehensive understanding of the hydrological impacts within the coexisting land use changes is needed. Here, we applied surface-groundwater-coupled simulations with historical river gauges and satellite observations to evaluate long-term and seasonal changes in Lancang-Mekong River Basin hydrology. Increasing irrigation elevated soil moisture but depleted groundwater storage. Conversely, deforestation reduced soil moisture, and increased lateral flow in areas with steep terrain compensated for groundwater depletion. Irrigation affected runoff by augmenting evapotranspiration and baseflow, which had opposite implications for runoff changes, causing a mixed spatial pattern of decreases and increases. Meanwhile, decreases in soil moisture due to deforestation offset increases in evapotranspiration due to irrigation, resulting in wider areas of runoff increases than decreases. These illustrate the distinct hydrological impacts of different land use changes and a pathway to complex system assessments.

Agricultural expansion leading to forest loss has significantly impacted climate, food, energy, and ecological systems[1-3]. The continuous expansion and intensified utilization of cropland have been driven by global population growth and regional economic development, and the expansion in irrigation has modified the surface and subsurface water balance[4,5]. In addition, the decreased forest cover and its effects on water sustainability[6] have been an important factor influencing freshwater security risks[7]. However, the hydrological influences and the underlying mechanisms of irrigation increases and the subsequent deforestation are unclear, and clarifying them is essential not only for research and resource management but also for national and global progress toward the United Nations' 2030 Sustainable Development Goals on food, water, and forest[8].

Systematically exploring and disentangling the influences of irrigation and deforestation on hydrological processes are still challenging because of the complex linkages and feedback between the water variables. Consequently, recent studies mostly focused on the influence of a single water variable or a specific aspect[4,6,9]. In the aspect of irrigation, soil moisture (SM) and evapotranspiration (ET) enhancements have been identified in regions

with irrigation, especially during the growing seasons[10,11]. Meanwhile, the groundwater storage (GW) and terrestrial water storage (TWS) depletions were driven by water overuse for heavy irrigation[5,12,13], which was likely to cause the spatiotemporal redistribution of streamflow and GW compared to natural conditions[14]. Accordingly, missing the linkages of different water variables limits our current understanding of irrigation's impact on the regional water cycle[4,14,15]. Moreover, a series of studies assessed the isolated effects of forest loss on runoff increments by using paired-watershed experiments[6], the empirical Budyko frameworks[9,16], and gauge observations combined with statistic models[17-19], which suggested that deforestation could additionally influence the water cycle when it was accompanied by irrigation.

To elucidate the impacts of irrigation and deforestation on the long-term changes in water cycle variables and clarify the underlying mechanisms, we set up a high-resolution (5 arcmin) and fully coupled model based on a set of climate, hydrological, and geological datasets for the Lancang-Mekong River Basin (LMRB) (Fig. S1). The LMRB is one of the largest river basins and is important for the livelihoods of over 70 million people[20]. In the

[1]School of Environmental Science and Engineering, Southern University of Science and Technology, Shenzhen, China. [2]Yellow River Research Institute, North China University of Water Resources and Electric Power, Zhengzhou, China. [3]Water, Environment, Processes and Analyses Division, BRGM—French Geological Survey, Orléans, France. [4]School of Environment and Civil Engineering, Dongguan University of Technology, Dongguan, China. [5]Earth Systems and Global Change group, Wageningen University and Research, Wageningen, The Netherlands. [6]Department of Earth System Science, Tsinghua University, Beijing, China. [7]Regional Climate Group, Department of Earth Sciences, University of Gothenburg, Gothenburg, Sweden. ✉e-mail: junguo.liu@gmail.com

LMRB, a fast growth phase of the irrigation expansion originated in the 1980s–1990s due to the rapid growth of population and rice export[21], leading to an accelerating deforestation rate[22,23]. Considering the large uncertainties derived from the lack of reservoir observations and actual operation rules[24], we selected the historical period of 1980–2010 for the focus of our investigation. To obtain spatiotemporally explicit information about the water cycle, we used the community water model (CWatM) coupled with the modular three-dimensional finite-difference groundwater flow (MOD-FLOW), hereafter referred to as CWatM-MODFLOW[25]. We calibrated it by simultaneously using site-based streamflow observations and the gridded satellite water storage product from Gravity Recovery and Climate Experiment (GRACE)[26,27] (Methods). The model was run for two land cover scenarios[28]. In the first scenario, the annual land cover was fixed as it was in 1980, labeled as the LAND_1980 experiment (exp). Comparably, the other scenario was designed as a control (CTRL) exp, in which the dynamic annual land cover change was simulated. As a result, the differences (denoted by Δ) between CTRL exp and LAND_1980 exp were caused by anthropogenic-induced vegetation changes and associated water use changes (Methods). Since the anthropogenic vegetation changes primarily manifested as different combinations of irrigation and deforestation, the grid cells were grouped into three types: irrigation increases with no deforestation (Irrigation(non-DF)), irrigation increases with deforestation (Irrigation(DF)), and no irrigation change (non-Irrigation) (Fig. 1). Our

findings suggest that the contrasting mechanisms and effects of irrigation and deforestation existed in different hydrological processes and differed in seasons.

Results

Widespread decreased correlation between *SM* and *GW*

The spatial distributions of the widespread deforestation and irrigation during 1980–2010 in the LMRB were inconsistent; that is, 25% of the grid cells exhibited a combination of deforestation and irrigation (i.e., Irrigation(DF)), and 13% of the grid cells exhibited an increase in irrigation without deforestation (i.e., Irrigation(non-DF)) (Fig. 1a). Within LAND_1980 exp, the correlation between the *SM* and the aridity index ($r_{(\text{Aridity index}, SM)}$) was generally positive, and so was the correlation between the *SM* and *GW* ($r_{(GW, SM)}$), with $r_{(\text{Aridity index}, SM)} > 0.5$ and $r_{(GW, SM)} > 0$ in 83% and 90% of the grid cells, respectively (Fig. 1b). The irrigation expansion caused widespread decreases in these correlations, shown by negative $\Delta r_{(\text{Aridity index}, SM)}$ and $\Delta r_{(GW, SM)}$ between CTRL exp and LAND_1980 exp, especially in southwestern parts where the irrigation was enhanced substantially (Fig. 1b–d). The Δr values were more negative in the Irrigation(non-DF) cells than in the Irrigation(DF) cells and non-Irrigation cells. The negative $\Delta r_{(GW, SM)}$ in the non-Irrigation cells suggests that the groundwater abstraction had an impact on the lateral groundwater flow (Fig. 1e).
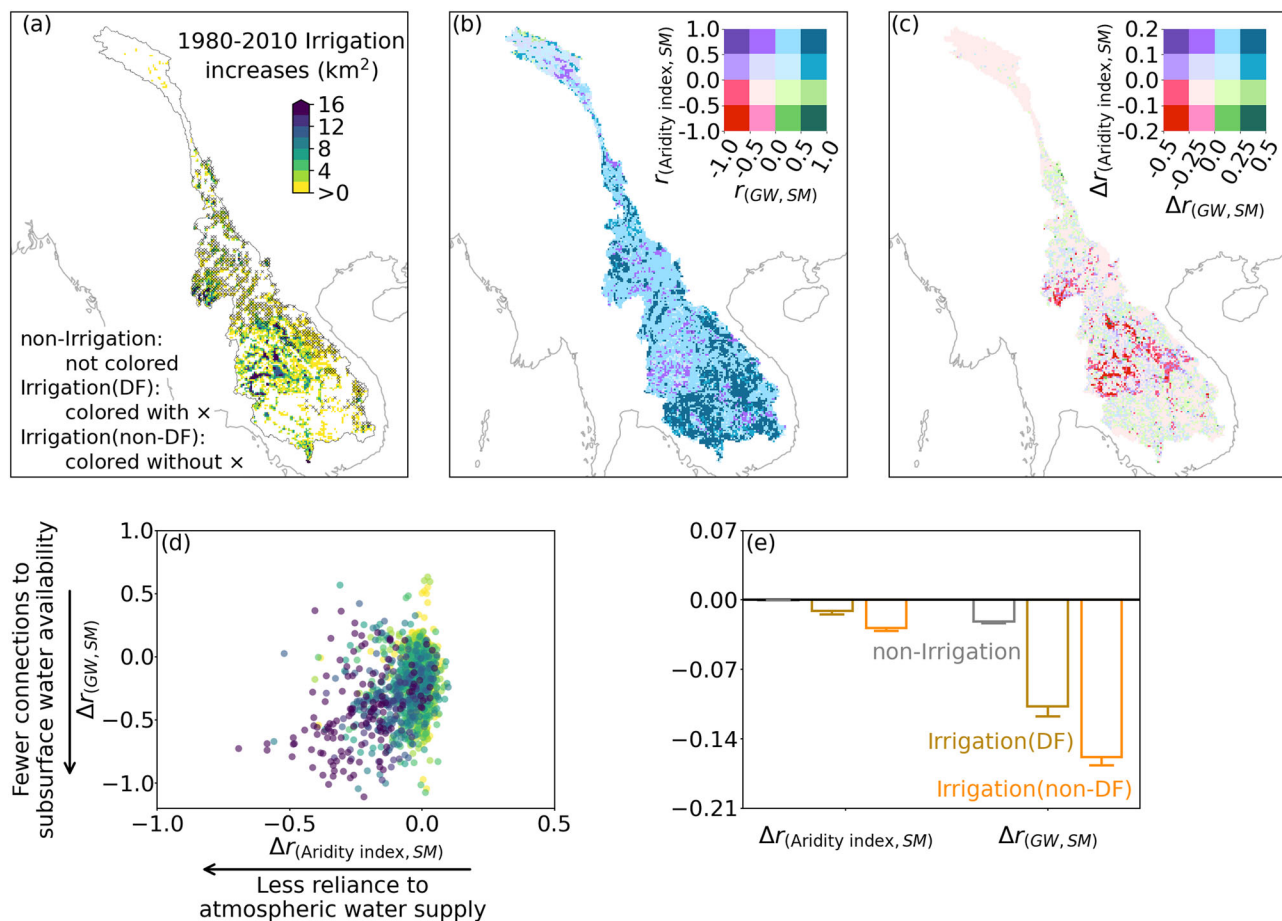

Fig. 1 | Weakened coupling due to irrigation increases and deforestation.
a Anthropogenic-induced vegetation changes during 1980–2010 in the Lancang-Mekong River Basin (LMRB) were grouped into three types: no irrigation change (non-Irrigation) and irrigation increases with or without deforestation (Irrigation(DF) or Irrigation(non-DF), respectively). **b–e** Consequently, the relationships between the aridity index and soil moisture (*SM*) and between the *SM* and groundwater storage (*GW*) were changed. The x symbol in (**a**) is shown at a 10 arcmin resolution for clear visualization, within which deforestation occurred in

at least one out of four 5 arcmin cells. **b** Kendall's rank correlation (*r*) in the LAND_1980 experiment (no land cover change since 1980). **c** Differences (Δ) in *r* between the control (CTRL) experiment and LAND_1980 experiment. In (**b**, **c**), the color of each grid indicates the co-occurrence of two (Δ)*r* values. *r* was computed from the annual values of aridity index, *SM*, and *GW*. The colors in (**d**) are tied to the levels of irrigation increases in (**a**), and the bars in (**e**) denote the mean and 95% confidence interval of the Δ*r* among the non-Irrigation, Irrigation(DF), and Irrigation(non-DF) grids.
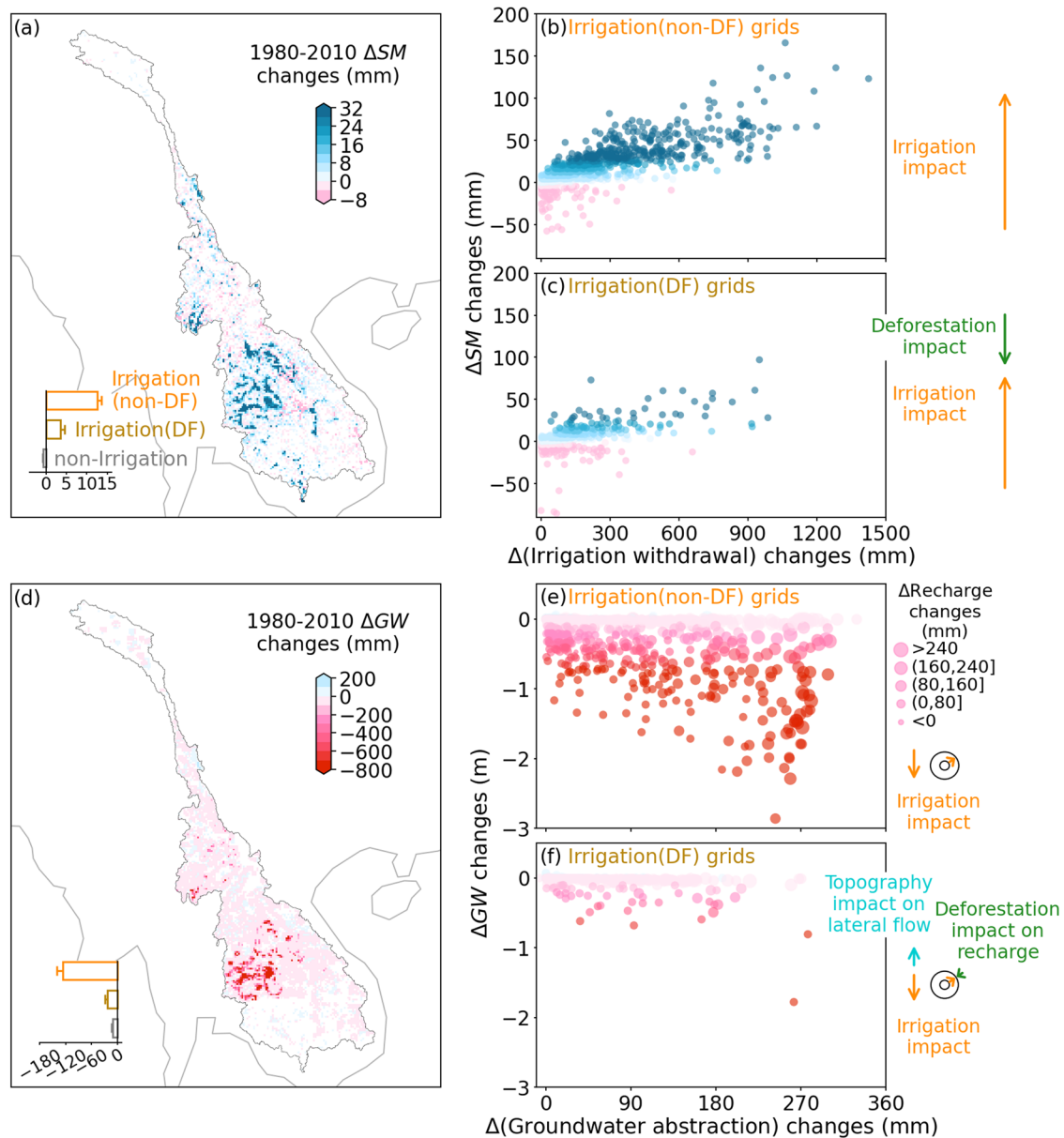
Fig. 2 | Long-term changes of *SM* and *GW* due to contrasting impacts of irrigation and deforestation. a, d The 31-year changes (the differences between CTRL exp and LAND_1980 exp) in the *SM* and *GW* for the Irrigation(non-DF), Irrigation(DF), and non-Irrigation grid cells in the LMRB. **b–c, e–f** Contrast in the impacts of irrigation and deforestation. The *SM*, *GW*, irrigation withdrawal, groundwater abstraction, and recharge are the yearly values used to calculate the changes based on the Sen's slope in each grid with a significant trend ($p < 0.05$) (Methods). The bars in the lower left corners of (**a, d**) denote the mean and 95% confidence interval among the Irrigation(non-DF), Irrigation(DF), and non-Irrigation grids. The colors in (**b, c**) are tied to (**a**), and those in (**e, f**) are tied to (**d**).

Impacts of irrigation and deforestation on the increase in *SM* and decrease in *GW*

Within the cells in which both correlations decreased, irrigation increased the *SM* and decreased the *GW* through abstraction (shown as positive ΔSM and negative ΔGW, respectively, in Fig. 2a, d). However, comparable variations in Δ(Irrigation withdrawal) could lead to more infiltrated water and greater ΔSM for the Irrigation(non-DF) cells than for the Irrigation(DF) cells because irrigation and deforestation had contrasting impacts (Figs. S2 and 2b, c). The reverse deforestation impact was evidenced by the lower infiltration and *SM* levels in the non-Irrigation grids with a lower forest fraction (Fig. S3). In addition, similar variations in the Δ(Groundwater abstraction) resulted in more negative ΔGW values in the Irrigation(non-DF) cells compared to the Irrigation(DF) cells (Fig. 2e, f). The mechanisms controlling this phenomenon include the following: 1) the steeper terrain in the locations with deforestation contributed to higher lateral groundwater

flow, compensating for *GW* decreases (Fig. S4); and 2) the deforestation itself reduced the recharge, enhancing the decreases in the *GW* (Fig. S3). It should be noted that irrigation could also have led to a slight increase in the baseflow (compared to the withdrawal rate) due to the increased recharge in the sub-grid groundwater cells unaffected by withdrawals (Fig. S5).

Impacts of irrigation and deforestation on changes in runoff

In contrast to *SM*, the ΔRunoff did not exhibit a consistent spatial pattern in the LMRB during 1980–2010 (Fig. 3a). By partitioning runoff into surface runoff and baseflow, results showed that Δ(Surface runoff) and ΔBaseflow contributed contrastingly, with respective positive and negative proportions, and the larger proportion of Δ(Surface runoff) than ΔBaseflow implies that the former dominated the ΔRunoff (Fig. 3b). The partial information decomposition (PID) was then applied, since the *SM* and *ET* have interactions and dependencies in controlling the surface runoff (Methods).
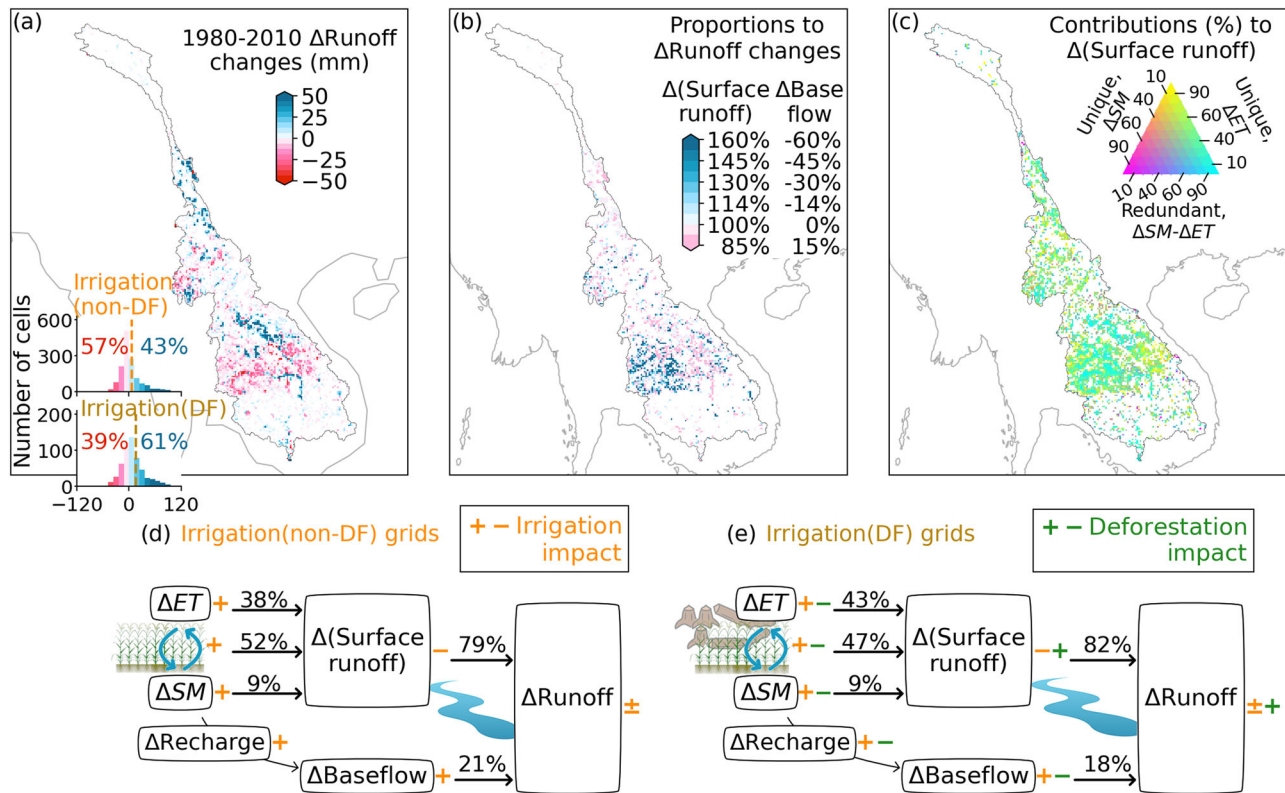
Fig. 3 | Long-term changes of runoff due to the contrasting impacts of irrigation and deforestation. a Changes in the runoff during the 31-year study period in the LMRB. **b** Proportions of Δ(Surface runoff) and ΔBaseflow, together with **c** contributions of the ΔSM and ΔET (namely, evapotranspiration) to the Δ(Surface runoff), reveal that **d–e** the inverse impacts of irrigation and deforestation on the different hydrological processes consequently enhanced the ΔRunoff. The calculations of the changes are the same as in Fig. 2. The percentages in the lower left corner of (**a**) are based on the number of positive/negative cells, and the dashed lines indicate the mean values. The proportions in (**b**) were calculated by dividing either the Δ(Surface runoff) or ΔBaseflow changes by the ΔRunoff changes. The contributions in **c** are based on the partial information decomposition, which quantifies the interactions and dependencies in a multivariate system (Methods). **d, e** show the average levels of contributions under the impacts of irrigation and deforestation.

The redundant information about ΔSM and ΔET, as well as the unique information about ΔET, largely contributed to the negative Δ(Surface runoff) changes (Fig. 3c), especially for the Irrigation(non-DF) cells (Fig. S5a–c). That is, the increases in ΔSM induced ΔET increases by supporting more crop transpiration and more ponded water evaporation in the expanded paddy areas, leading to the decreases in Δ(Surface runoff) (Figs. S6 and 3d). Therefore, with the converse increases in ΔBaseflow, the ΔRunoff in the Irrigation(non-DF) grids exhibited a mixed pattern of 57% grid cells in decreases and 43% grid cells in increases (Figs. S5d–f and 3a).

For the Irrigation(DF) grids with a combination of irrigation and deforestation, the Δ(Surface runoff) was dominated by unique or redundant information about ΔET and tended to be more positive than the situation for Irrigation(non-DF) (Figs. 3c and S5a–c). This is attributed to the above finding that the increases in ΔSM were lower in the Irrigation(DF) grids than in the Irrigation(non-DF) grids, causing less ΔET increases from both perspectives of transpiration and evaporation (Figs. 2a and S6). Consequently, although deforestation simultaneously alleviated the decreases in Δ(Surface runoff) and the increases in ΔBaseflow caused by irrigation (Fig. 3e), the ΔRunoff was primarily influenced by the fact that the surface runoff predominantly increased (Fig. 3a).

Exceptional impacts of irrigation and deforestation in summer
From the perspective of seasonality, we found that the ΔRunoff influenced by irrigation changed from positive to negative during summer months, after which it returned to positive (Fig. 4a). The ΔRunoff was mainly due to the seasonal Δ(Surface runoff), except for the elevated contribution of the ΔBaseflow, which alleviated the decrease in the ΔRunoff during summer

(Figs. 4b and S7d). In addition, the Δ(Surface runoff) was mainly controlled by the ΔET that was increased by the ΔSM (Fig. S7a–b), since the redundant information about ΔSM and ΔET made the largest contribution (Fig. 4c).

Compared to the Irrigation(non-DF) grids, the decreases in ΔRunoff in summer were intensified in the Irrigation(DF) grids (Fig. 4a) because of the lower increases in ΔBaseflow in the Irrigation(DF) grids (Fig. S7d); however, the increases in ΔRunoff were greater in the other months, which eventually caused more grids with positive ΔRunoff changes (Figs. 4a and 3a). These greater increases in ΔRunoff, which were dominated by the Δ(Surface runoff), were mainly caused by the lower increases in ΔET and its driver, ΔSM (Figs. 4b–d and S7a–b). Exceptionally, the ΔSM among Irrigation(DF) grids show opposite changes to that of Irrigation(non-DF) grids in summer because the irrigation during crop growing seasons increased the ΔSM but deforestation countered the impact of the irrigation (Fig. S7a).

Discussion
The widespread high correlation between the $r_{\text{(Aridity index, SM)}}$ and $r_{\text{(GW, SM)}}$ in the LAND_1980 exp during 1980–2010 in the LMRB (Fig. 1) indicates that precipitation was the major source of the SM and the correlation between the GW and SM was stable when the regional water cycles were not affected by irrigation and deforestation. Such high correlations between the aridity index and SM (>0.6) have also been identified in different parts of the world, particularly in the western Europe and the southern United States, which have experienced a wetting trend of precipitation in recent decades (1991–2019)[29]. In addition, site-based observations of water table depths[30] and observation-validated groundwater simulations[31] have revealed that there were highly positive

Fig. 4 | Seasonal variability of the runoff changes under the impacts of irrigation and deforestation. **a** Seasonal variability of ΔRunoff. **b** Contributions of Δ(Surface runoff) and ΔBaseflow to ΔRunoff. **c–d** Contributions of ΔSM and ΔET to Δ(Surface runoff) in the LMRB during 1980–2010. Unlike Fig. 3, the ΔRunoff in (**a**) was calculated using the daily ΔRunoff during the 31-year study period on the same day, and each ΔRunoff of a day is the average among the Irrigation(non-DF)/Irrigation(DF)/non-Irrigation grid cells.
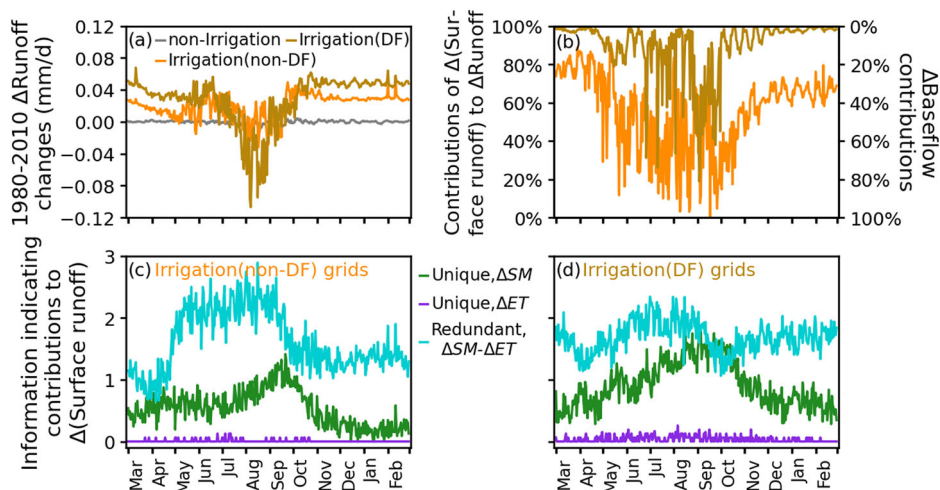
correlations between the groundwater level and SM in regions where groundwater is an important source for buffering the reliance of SM on precipitation. Therefore, the widespread negative Δ$r_{(Aridity index, SM)}$ and Δ$r_{(GW, SM)}$ values suggest that the increase in irrigation could decrease the reliance of SM on the aridity index and could disturb the relationship between the GW and SM (Fig. 1).

Notably, we found that the impacts of deforestation and irrigation on the SM and GW were different. (1) The irrigation expansion increased the SM, while the deforestation decreased the SM. (2) The increase in the irrigation-induced groundwater abstraction reduced the GW and the recharge changed by lower forest area boosted the decrease in the GW (Fig. 2). The irrigation impact was conducted by exploitation of GW and provided additional water to increase the SM and recharge in the irrigated cells[4,14,25,32]. In contrast, deforestation with lower tree density, resulting in less dense roots and organic matter (from litter), would reduce the water infiltration and water-holding capacity of the soil and consequently reduce the recharge and baseflow[33,34]. Furthermore, our findings demonstrate the positive dependency of ET (specifically, transpiration) to SM in water-limited regions[35,36] (Fig. S6), differently from energy-limited watersheds in Brazil where increased SM was a negative response to decreased ET rates by deforestation[37]. In this context, the hydrological mechanisms of irrigation expansion via deforestation were elucidated by isolating and comparing the impacts of irrigation and deforestation.

The occurrence of the spatially inconsistent ΔRunoff in the Irrigation(non-DF) grid cells highlights not only the contrasting impacts of the increases in the ΔSM and ΔET on the Δ(Surface runoff) but also the contrasting impacts of the decreases in Δ(Surface runoff) and increases in ΔBaseflow (Fig. 3). Building upon the general notion that increasing SM benefits runoff generation while increasing ET decreases the amount of water available for the formation of runoff[4,38], we determined that the ΔET via positive SM-transpiration coupling and the ΔET enhanced by water evaporation on the saturated SM of the expanded paddy areas were the main factors controlling the Δ(Surface runoff) in the context of irrigation expansion[9,39]. Moreover, widespread increases in recharge and baseflow during irrigation expansion, which have also been observed in other basins in which irrigation is utilized[32,40], could buffer runoff deficits predominantly caused by decreases in surface runoff in most grids or increased runoff in other grids due to increased surface runoff. This resulted in an almost half-and-half mix pattern of both decreases and increases.

The impact of the decreases in forest cover on the increases in runoff (Fig. 3) is supported by the sensitivity calculations of the Budyko assumption for global runoff dataset[16], statistical analyses of streamflow records[18,19], and watershed modeling[37]. From this perspective, in the study area, the deforestation conducted to achieve irrigation expansion led to additional surface runoff beyond that caused by irrigation (Figs. 3 and S5), except for the

summer when irrigation caused runoff deficits (Fig. S7). This is consistent with observations of other large river basins in Brazil[17]. Moreover, deforestation led to decreased recharge and baseflow due to alteration of the soil structure, which further exacerbated the runoff deficit (Figs. 4 and S7). In the other months, the ΔRunoff, which was predominantly caused by the Δ(Surface runoff), was increased by irrigation, and deforestation decreased the ΔET, thus leading to a greater increase in the ΔRunoff. Overall, the impact of deforestation on ΔRunoff was in contrast with that of irrigation via different mechanisms for different seasons, shifting to the runoff pattern with more long-term increases.

By identifying those potential mechanisms by which irrigation and deforestation impact surface and subsurface hydrological processes contrastingly, this study enhanced our understanding of how and why the pivotal water variables (like SM, GW, ET, baseflow, runoff) could be changed in the long term and between the seasons, and what were the connections between variables. The findings could benefit the broader investigations in other water-limited regions[35], especially under the context that widespread shifts from energy-limited to water-limited conditions were projected due to climate change[36]. The changing climate also affected baseflow through the changes in precipitation, evaporative demand and snow fraction[41]. Further assessments of human-natural water systems were suggested by taking into account more reliable reservoir operation information[24] and dynamic farmer decisions interacted with the hydrological environment[42]. Additionally, based on multi-source observation adjustments and numerical experiments, our approaches hold practical applicability on a global scale[28], and the multivariate analysis framework could be adapted to other complex systems[43].

Methods
Model setup and forcing data
The CWatM is a physics-based large-scale hydrological model that includes human impacts such as irrigation, water withdrawal for other purposes, surface reservoirs, and land cover[44]. CWatM-MODFLOW further allows the modeling of groundwater lateral flow, groundwater exchanges with surface soil and water, and groundwater pumping[25]. Surface water-groundwater exchanges are characterized by (1) groundwater recharge from the CWatM to MODFLOW and (2) groundwater capillary rise and baseflow simulated by MODFLOW to the lower soil layer and the river network system in CWatM. The land cover changes are characterized using the six classes[44], and the groundwater abstraction was calculated based on the water demands for livestock, industry, domestic use[44], and irrigation[25].

We applied CWatM-MODFLOW to the LMRB using high resolutions of 5 arcmin (~9 km at the Equator) for CWatM and 1.5 km for MOD-FLOW. Within the coupled model, the simulations were applied at time steps of 1 day and 1 week for CWatM and MODFLOW, respectively.

Regarding driving the model at a high resolution, we used a regional climate product for 1980−2010[45]. This recently developed product was derived using the Weather Research and Forecasting (WRF) model to dynamically downscale the 0.25° fifth generation of the European Centre for Medium-Range Weather Forecasts (ECMWF) atmospheric reanalysis of the global climate (ERA5) global data to 9 km in East Asia. It has a reliable representation compared with other products and has been validated using gauge and satellite observations[45]. The forcing datasets were resampled to a resolution of 5 arcmin.

Regional parameterization

The regional parameterizations were improved in both the CWatM and MODFLOW parts. For CWatM, the unsaturated hydraulic conductivity in the soil layers (K; m d^{-1}) was determined using the van Genuchten equation[46] (Eq. (1)) based on the soil saturated conductivity (K_s; m d^{-1}), the actual, maximum, and residual amounts of SM (θ, θ_s, and θ_r, respectively, in cm^3 cm^{-3}), a pore-size related parameter (m), and an empirical shape factor (l)[44,47], as follows:

$$K = K_s \left(\frac{\theta - \theta_r}{\theta_s - \theta_r}\right)^l \left\{1 - \left[1 - \left(\frac{\theta - \theta_r}{\theta_s - \theta_r}\right)^{1/m}\right]^m\right\}^2 \quad (1)$$

where K_s, θ, θ_s, θ_r, and m, provided in the CWatM default maps, were calculated based on the soil properties from the Harmonized World Soil Database 1.2[48] and the pedotransfer functions from the Hydraulic Properties of European Soils (HYPRES)[49]. However, we found that the range of the provided m for our study area exceeds the lower limit of 0.5[50], causing K to remain at low levels and the fluxes of the percolation in the groundwater recharge to be much lower than the preferential flow (Fig. S8). The study in the North China Plain[51] adjusted the magnitude of the percolation within the groundwater recharge using an exponential equation with a calibrated site-specific parameter α instead of Eq. (1) (see examples of K-θ curves in Fig. S8) based on an earlier field investigation in their study region[52]. In contrast to their attempts, the parameters of Eq. (1) for the LMRB refer to HiHydroSoil v2.0[53], which applies pedotransfer functions based on thousands of soil samples and performs significantly better than HYPRES[54]. Moreover, l, which was originally interpreted as a physical parameter related to the tortuosity structure of the connected pores[55], was found to always be lower than its predetermined value of 0.5 in further studies[47,56], providing flexibility to compensate for a conceptual deficiency of the capillary bundle models[57]. Therefore, l was adjusted to an appropriate value during the calibration to accurately predict K in groundwater-soil exchanges[58].

For MODFLOW, the upward flow from the groundwater system to the soil layer and channels of CWatM was calculated by using DRN package, which was determined by simulated water table depth and permeability in each cell. Then, the partitioning of upward groundwater flow into capillary rise feeding the soils and baseflow feeding the rivers was conducted by computing 500 m resolution river networks with a flow accumulation area threshold of 25 km[259] based on the 3 arcs (~90 m at the Equator) hydrologically conditioned digital elevation model (C-DEM) of HydroSHEDS[60]. This partitioning was further calibrated for each catchment by adding an adjusted factor[25]. The aquifer permeability and porosity were obtained from global hydrogeology maps 2.0 (GLHYMPS 2.0)[61]. In addition, we improved the identification of permafrost distribution using the new dataset based on comprehensive field data[62] (Fig. S1), and we conceptualized the permafrost as an aquitard layer with a low hydraulic conductivity of 5.2×10^{-11} m/s[63,64]. The specific yield is close to the porosity for aquifers with a large grain size, but it is much smaller than the porosity for aquifers with a small grain size[65]. Therefore, the specific yield was approximated to be 80% of the porosity for sand and larger grain sizes, and this reduction scale was calibrated for slit and clay[66].

Based on a limited geological survey[67] and our study's purpose of surface water-groundwater interactions[68,69], we considered one unconfined aquifer layer with varying thicknesses from the mountains to sediments for sub-basins 1–10 (Fig. S1)[70]. In contrast, sub-basin 11, which is mainly located in the Cambodia Mekong River Delta aquifer, was considered to be a confined aquifer[71], and we applied a global field data-based relationship between the specific storage and porosity to characterize the specific storage[72]. The method of determining the aquifer thickness distribution[70] was embedded in the model. Accordingly, the elevation differences (E) in the C-DEM along the drainage direction network from the hydrological data and maps based on shuttle elevation derivatives at multiple scales (HydroSHEDS) database were used to classify the cells into alluvial aquifer and mountain range aquifer cells. The relative differences (E') normalized from E (Eq. (2)) were used to rate the z-scores (Z in Eq. (3)), which indicate the likelihood that the alluvial aquifer cells form a thick layer close to the river or a thinner layer farther away from the steam[70].

$$E' = 1 - \frac{E - E_{min}}{E_{max} - E_{min}} \quad (2)$$

$$Z = G^{-1}(E') \quad (3)$$

where G^{-1} is the inverse standard normal distribution, and the mapping of Z was combined with a log-normal distribution of thickness values with a randomly sampled average (A) and a fixed coefficient of variation (C_v) (Eq. (4))[69,70].

$$\text{thickness} = e^{ln(A)\left(1 + C_v Z\right)} \quad (4)$$

where A was adjusted during the calibration, and the mountain range cells, which mainly consisted of hard rock with secondary permeability, were assumed to have only a thin aquifer below the soil layers with the fifth percentile of the thickness distribution.

Calibration scheme and model performance

The LMRB was divided into 11 independent sub-basins based on the locations of the hydrological station and the drainage direction (Fig. S1), and each sub-basin had different parameters for characterizing the spatial heterogeneity within this large river basin[73]. For each sub-basin, we calibrated and validated the model using the daily discharge at the gauge station locations and the monthly TWS anomalies among the sub-basin cells. The calibration and validation periods were 2002−2006 and 2007−2010, respectively (Table S1), as the GRACE TWS datasets are available from 2002 and the operations of hydropower dams after 2010 would obscure the focus of this research. The calibration was performed using non-dominated sorting genetic algorithm II (NSGA-II) to evolve the 14 parameters associated with snowmelt, crop evapotranspiration, open water evaporation, exchanges between soil and groundwater, soil depth, interflow, infiltration, preferential flow, groundwater recharge, runoff concentration and routing, reservoir and lake storage, and aquifer thickness distribution. Three objective functions were utilized to obtain the Pareto-optimal solutions: (1) the modified Kling-Gupta efficiency (KGE_{dis}) between the simulated and observed discharge[26,74], (2) the correlation coefficient (r'_{TWS}), and 3) the root mean square error ($RMSE_{TWS}$) between the simulated and observed TWS anomalies[51,75], where the r'_{TWS} and $RMSE_{TWS}$ scores were integrated from the grid level to the sub-basin level to achieve consistency with KGE_{dis} (see the following methods).

The scarce valuable gauge discharge data have long been a primary concern for LMRB research and resource management[20,76]. In contrast, the satellite-observed TWS data, as a reliable constraint that improves watershed simulations, were integrated considering variables such as the GW and SM[26,77]. Accordingly, the KGE_{dis} had a higher weight of 0.7 for the fitness comparisons in NSGA-II, compared to the other two objectives that need to be maximized (i.e., r'_{TWS} and 1-$RMSE_{TWS}$). Although the r'_{TWS} and $RMSE_{TWS}$ are comparable in terms of importance, we found that the r'_{TWS}, which exhibited larger variations, had higher sensitivity for the Pareto multi-optimization, so their weights were set to 0.2 and 0.1, respectively. These weights were also used to determine the metric (M) for selecting the optimal

parameters among the Pareto frontiers (Eq. (5)), as follows:

$$M = 0.7 \times KGE_{dis} + 0.2 \times r'_{TWS} + 0.1 \times (1 - RMSE_{TWS}) \quad (5)$$

where r'_{TWS} and $RMSE_{TWS}$ were calculated in each 0.5° cell and then averaged for each sub-basin, consistent with KGE_{dis}. The observed TWS anomalies at a 0.5° resolution were the ensemble mean of the Jet Propulsion Laboratory mass concentration (mascon) product (0.5° resolution)[78] and the Center for Space Research mascon product (0.25° resolution)[79] following the recent study[80]. The simulated TWS anomalies were implemented with an area-based upscaling from 5 arcmin to 0.5° during the calibrations. Such a multi-objective calibration strategy has been proven to have the ability to decrease the equifinality of the parameterization and reduce the uncertainties of hydrological predictions[26,27].

The NSGA-II was set up with a population size of 256, a recombination pool size of 80, and 60 generations to ensure convergence. For each set of parameters, the CWatM-MODFLOW was used to conduct a warmup run for 20 years using the daily average meteorological forcing for 1980−2010 20 times, which proved to be sufficient to initialize the water table[25,51,81]. Since the hydrologic predictions for each sub-basin were largely impacted by the discharge from the upstream area of each sub-basin, the calibration and validation were employed consecutively from the upstream sub-basins to the downstream sub-basins. The overall performance is shown in Fig. S1b, which shows that our multi-objective parameter optimization method can provide a robust representation of both the surface and subsurface hydrological processes. We found that the performance of the TWS simulations was poor for the first sub-basin (Fig. S9), which was probably because the parameterization of the groundwater system in this region was data-limited and had large uncertainties. Fortunately, this region was not the primary focus of the analysis in this research.

Experimental design and data analysis
The hydrological model was run for two land cover scenarios[28], namely LAND_1980 exp and CTRL exp. Accordingly, Δ values in each of the variables were the differences between CTRL exp and LAND_1980 exp, reflecting the impacts of deforestation and irrigation on the water cycle, and these impacts occurred in different combinations among the grid cells: Irrigation(non-DF), Irrigation(DF), and non-Irrigation.

Kendall's rank correlation, which avoids linearity assumptions, was applied to identify the relationships between the aridity index and SM (denoted as $r_{(Aridity\ index,\ SM)}$) and between the GW and SM (denoted as $r_{(GW,\ SM)}$)[19,36]. The aridity index was calculated as the ratio of precipitation to potential evapotranspiration, representing the hydro-climatic conditions that could control the SM[82], and the variabilities of the GW and SM were found to be consistent in different hydro-climatic conditions[83,84]. In Figs. 1–3, the aridity index is based on the annual amounts of precipitation and potential evapotranspiration, which were summed using the daily simulated values, and the SM and GW are the annual averages of the daily simulated values. After calculating these values in each grid of the LAND_1980 exp and CTRL exp, the change in r (i.e., $\Delta r_{(Aridity\ index,\ SM)}$ or $\Delta r_{(GW,\ SM)}$) was obtained by subtracting the values of LAND_1980 exp from those of CTRL exp. Therefore, the Δr was positive when r was higher in CTRL than in LAND_1980.

The long-term changes in the variables (e.g., ΔSM and ΔGW) were calculated based on a non-parametric estimation method (Eq. (6))[76] for each grid and each day. In Figs. 2 and 3, the changes were calculated in each grid for the annual averages of the SM and GW and the annual amounts of the irrigation withdrawal, groundwater abstraction, recharge, baseflow, surface runoff, evapotranspiration, and runoff. The recharge is defined as the net groundwater recharge from the soil (i.e., recharge minus capillary flow). In addition to showing these overall changes during the study period (1980–2010), the changes shown in Fig. 4 demonstrate that the seasonal variability was calculated based on the daily Δ values (e.g., ΔRunoff) over the 31-year period on the same day, where each Δ value for a day was the average among each type of grid cell (Irrigation(non-DF)/Irrigation(DF)/non-

Irrigation), given by

$$\Delta\ \text{change} = k \times n \quad (6)$$

where n is the number of years in the study period, i.e., 31, k is the Sen's slope estimated for each grid or each day (mm/yr or mm/d) based on the 31 Δ values for each variable. Sen's slope estimates the trend of a time series by applying the slope of the Kendall-Theil robust line, and it has been widely used to describe the magnitudes of the trends of climate and hydrological variables. The Mann-Kendall test was conducted at a significance level of 95% for the overall changes.

As runoff consists of surface runoff and baseflow, the ratios of either |Δ(Surface runoff)| or |ΔBaseflow| to |Δ(Surface runoff)|+|ΔBaseflow| were used to quantify their respective contributions to the ΔRunoff changes[85]. In contrast, the ΔSM and ΔET have interactions and dependencies in controlling the Δ(Surface runoff)[38], so their contributions in such a multivariate system were quantified by employing partial information decomposition (PID)[43]. PID measures the amount of information that the ΔSM or ΔET uniquely contributes to the Δ(Surface runoff), the redundant information between ΔSM and ΔET, and the synergistic information (Eq. (7)).

$$I(\Delta SM - \Delta ET; \Delta(\text{Surface runoff})) = U(\Delta SM; \Delta(\text{Surface runoff}))$$
$$+ U(\Delta ET; \Delta(\text{Surface runoff})) + R(\Delta SM - \Delta ET; \Delta(\text{Surface runoff}))$$
$$+ S(\Delta SM - \Delta ET; \Delta(\text{Surface runoff}))$$

$$(7)$$

where I is the total mutual information, and U, R, and S are the unique, redundant, and synergistic information, respectively. The computation was conducted using the method of refs. 43,86, and the unique, redundant, and synergistic contributions of the ΔSM and ΔET to the ΔRunoff variability were U/I, R/I, and S/I, respectively. The unique ΔSM and ΔET information reflects the direct contributions of the irrigation-induced and/or deforestation-induced ΔSM and ΔET variations to the Δ(Surface runoff), respectively, while the redundant information reflects the contributions of the coupled variations in ΔSM and ΔET to the Δ(Surface runoff)[43]. When the Δ(Surface runoff) increased and the redundant information made the largest contribution, we assumed that the increase in the ΔSM drove the Δ(Surface runoff), although there was negative feedback between the ΔSM and ΔET. In contrast, when the Δ(Surface runoff) decreased and the redundant information made the largest contribution, the increase in the ΔET induced by the increase in the ΔSM contributed to the Δ(Surface runoff).

Data availability
The forcing datasets[45] are available from http://biggeo.gvc.gu.se/TPReanalysis/. The HiHydroSoil v2.0[53], HydroSHEDS C-DEM[60], and GLHYMPS 2.0[61] for parameterization are available from https://www.futurewater.eu/projects/hihydrosoil/, https://www.hydrosheds.org/hydrosheds-core-downloads, and https://borealisdata.ca/dataset.xhtml?persistentId=doi:10.5683/SP2/TTJNIU, respectively. The discharge data is from the Mekong River Commission (MRC) website (https://portal.mrcmekong.org/). The Jet Propulsion Laboratory mascon product[78] and the Center for Space Research mascon product[79] for TWS anomalies are available from https://grace.jpl.nasa.gov/data/get-data/ and https://www2.csr.utexas.edu/grace/RL06_mascons.html, respectively.

Code availability
The CWatM-MODFLOW model[25] and the pre-processing code for groundwater parameterization are available on Zenodo (https://doi.org/10.5281/zenodo.6609072). The multi-objective calibration method based on NSGA-II can be accessed in the tutorial files on GitHub (https://github.com/iiasa/CWatM). A demo to implement the PID method[86] is also available from GitHub (https://github.com/pwollstadt/IDTxl).

References

1. Betts, M. G. et al. Global forest loss disproportionately erodes biodiversity in intact landscapes. *Nature* **547**, 441–444 (2017).
2. Feng, Y. et al. Doubling of annual forest carbon loss over the tropics during the early twenty-first century. *Nat. Sustain.* **5**, 444–451 (2022).
3. Hoang, N. T. & Kanemoto, K. Mapping the deforestation footprint of nations reveals growing threat to tropical forests. *Nat. Ecol. Evol.* **5**, 845–853 (2021).
4. McDermid, S. et al. Irrigation in the Earth system. *Nat. Rev. Earth Environ.* **4**, 435–453 (2023).
5. Scanlon, B. R. et al. Global water resources and the role of groundwater in a resilient water future. *Nat. Rev. Earth Environ.* **4**, 87–101 (2023).
6. McDonnell, J. J. et al. Water sustainability and watershed storage. *Nat. Sustain.* **1**, 378–379 (2018).
7. Mekonnen, M. M. & Hoekstra, A. Y. Four billion people facing severe water scarcity. *Sci. Adv.* **2**, e1500323 (2016).
8. UN General Assembly. Transforming our world: the 2030 Agenda for Sustainable Development. https://sdgs.un.org/2030agenda (2015).
9. Destouni, G., Jaramillo, F. & Prieto, C. Hydroclimatic shifts driven by human water use for food and energy production. *Nat. Clim. Change* **3**, 213–217 (2012).
10. Lawston, P. M., Santanello, J. A. & Kumar, S. V. Irrigation Signals Detected From SMAP soil moisture retrievals. *Geophys. Res. Lett.* **44**, 11860–11867 (2017).
11. Pascolini-Campbell, M., Fisher, J. B. & Reager, J. T. GRACE-FO and ECOSTRESS synergies constrain fine-scale impacts on the water balance. *Geophys. Res. Lett.* **48**, e2021GL093984 (2021).
12. Condon, L. E. & Maxwell, R. M. Groundwater-fed irrigation impacts spatially distributed temporal scaling behavior of the natural system: a spatio-temporal framework for understanding water management impacts. *Environ. Res. Lett.* **9**, 034009 (2014).
13. Scanlon, B. R. et al. Groundwater depletion and sustainability of irrigation in the US High Plains and Central Valley. *Proc. Natl Acad. Sci. USA* **109**, 9320–9325 (2012).
14. Kustu, M. D., Fan, Y. & Robock, A. Large-scale water cycle perturbation due to irrigation pumping in the US High Plains: A synthesis of observed streamflow changes. *J. Hydrol.* **390**, 222–244 (2010).
15. Zaerpour, M. et al. Impacts of agriculture and snow dynamics on catchment water balance in the U.S. and Great Britain. *Commun. Earth Environ.* **5**, 733 (2024).
16. Zhou, G. et al. Global pattern for the effect of climate and land cover on water yield. *Nat. Commun.* **6**, 5918 (2015).
17. Chagas, V. B. P., Chaffe, P. L. B. & Bloschl, G. Climate and land management accelerate the Brazilian water cycle. *Nat. Commun.* **13**, 5136 (2022).
18. Levy, M. C., Lopes, A. V., Cohn, A., Larsen, L. G. & Thompson, S. E. Land use change increases streamflow across the arc of deforestation in Brazil. *Geophys. Res. Lett.* **45**, 3520–3530 (2018).
19. Zhang, M. et al. A global review on hydrological responses to forest change across multiple spatial scales: Importance of scale, climate, forest type and hydrological regime. *J. Hydrol.* **546**, 44–59 (2017).
20. Liu, J., Chen, D., Mao, G., Irannezhad, M. & Pokhrel, Y. Past and future changes in climate and water resources in the Lancang–Mekong river basin: current understanding and future research directions. *Engineering* **13**, 144–152 (2022).
21. MRC. *Final Report Agricultural Land Use Monitoring (Pilot study in the Selected Areas in each member country)*. (MRC Secretariat, 2020).
22. Chen, A., Chen, A., Varis, O. & Chen, D. Large net forest loss in Cambodia's Tonle Sap Lake protected areas during 1992-2019. *Ambio* **51**, 1889–1903 (2022).
23. Zeng, Z. Z. et al. Highland cropland expansion and forest loss in Southeast Asia in the twenty-first century. *Nat. Geosci.* **11**, 556–562 (2018).
24. Wang, Y. M., Long, D. & Li, X. D. High-temporal-resolution monitoring of reservoir water storage of the Lancang-Mekong River. *Remote Sens. Environ.* **292**, 113575 (2023).
25. Guillaumot, L. et al. Coupling a large-scale hydrological model (CWatM v1.1) with a high-resolution groundwater flow model (MODFLOW 6) to assess the impact of irrigation at regional scale. *Geosci. Model Dev.* **15**, 7099–7120 (2022).
26. Bai, P., Liu, X. M. & Liu, C. M. Improving hydrological simulations by incorporating GRACE data for model calibration. *J. Hydrol.* **557**, 291–304 (2018).
27. Dembélé, M., Hrachowitz, M., Savenije, H. H. G., Mariéthoz, G. & Schaefli, B. Improving the predictive skill of a distributed hydrological model by calibration on spatial patterns with multiple satellite data sets. *Water Resour. Res.* **56**, e2019WR026085 (2020).
28. Humphrey, V. et al. Soil moisture-atmosphere feedback dominates land carbon uptake variability. *Nature* **592**, 65–69 (2021).
29. Ullah, S. et al. Spatiotemporal changes in global aridity in terms of multiple aridity indices: an assessment based on the CRU data. *Atmos. Res* **268**, 105998 (2022).
30. McMillan, H. K. & Srinivasan, M. S. Characteristics and controls of variability in soil moisture and groundwater in a headwater catchment. *Hydrol. Earth Syst. Sci.* **19**, 1767–1786 (2015).
31. Martínez-de la Torre, A. & Miguez-Macho, G. Groundwater influence on soil moisture memory and land–atmosphere fluxes in the Iberian Peninsula. *Hydrol. Earth Syst. Sci.* **23**, 4909–4932 (2019).
32. Zhang, Y. K. & Schilling, K. E. Increasing streamflow and baseflow in Mississippi River since the 1940s: effect of land use change. *J. Hydrol.* **324**, 412–422 (2006).
33. Tyagi, J. V., Qazi, N., Rai, S. P. & Singh, M. P. Analysis of soil moisture variation by forest cover structure in lower western Himalayas, India. *J. Forestry Res.* **24**, 317–324 (2013).
34. Vereecken, H. et al. Soil hydrology in the Earth system. *Nat. Rev. Earth Environ.* **3**, 573–587 (2022).
35. Hsu, H. & Dirmeyer, P. A. Deconstructing the soil moisture-latent heat flux relationship: the range of coupling regimes experienced and the presence of nonlinearity within the sensitive regime. *J. Hydrometeorol.* **23**, 1041–1057 (2022).
36. Denissen, J. M. C. et al. Widespread shift from ecosystem energy to water limitation with climate change. *Nat. Clim. Change* **12**, 677–684 (2022).
37. Guimberteau, M. et al. Impacts of future deforestation and climate change on the hydrology of the Amazon Basin: a multi-model analysis with a new set of land-cover change scenarios. *Hydrol. Earth Syst. Sci.* **21**, 1455–1475 (2017).
38. Li, W. et al. Contrasting drought propagation into the terrestrial water cycle between dry and wet regions. *Earth's. Future* **11**, e2022EF003441 (2023).
39. Jaramillo, F. & Destouni, G. Local flow regulation and irrigation raise global human water consumption and footprint. *Science* **350**, 1248–1251 (2015).
40. Bouimouass, H., Fakir, Y., Tweed, S. & Leblanc, M. Groundwater recharge sources in semiarid irrigated mountain fronts. *Hydrol. Process.* **34**, 1598–1615 (2020).
41. Zaerpour, M. et al. Climate shapes baseflows, influencing drought severity. *Environ. Res. Lett.* **20**, 014035 (2024).
42. de Bruijn, J. A. et al. GEB v0.1: a large-scale agent-based socio-hydrological model – simulating 10 million individual farming households in a fully distributed hydrological model. *Geosci. Model Dev.* **16**, 2437–2454 (2023).
43. Maina, F. Z., Kumar, S. V., Albergel, C. & Mahanama, S. P. Warming, increase in precipitation, and irrigation enhance greening in High Mountain Asia. *Commun. Earth Environ.* **3**, 43 (2022).

44. Burek, P. et al. Development of the Community Water Model (CWatM v1.04) - a high-resolution hydrological model for global and regional assessment of integrated water resources management. *Geosci. Model Dev.* **13**, 3267–3298 (2020).

45. Ou, T. H. et al. Wet bias of summer precipitation in the northwestern Tibetan Plateau in ERA5 is linked to overestimated lower-level southerly wind over the plateau. *Clim. Dyn.* **61**, 2139–2153 (2023).

46. van Genuchten, M. T. A closed-form equation for predicting the hydraulic conductivity of unsaturated soils. *Soil Sci. Soc. Am. J.* **44**, 892–898 (1980).

47. Schaap, M. G. & Leij, F. J. Improved prediction of unsaturated hydraulic conductivity with the Mualem-van Genuchten model. *Soil Sci. Soc. Am. J.* **64**, 843–851 (2000).

48. Fischer, G. et al. *Global agro-ecological zones assessment for agriculture (GAEZ 2008)*. (IIASA, Laxenburg, Austria and FAO, Rome, Italy, 2008).

49. Wösten, J. H. M., Lilly, A., Nemes, A. & Le Bas, C. Development and use of a database of hydraulic properties of European soils. *Geoderma* **90**, 169–185 (1999).

50. Vogel, T., van Genuchten, M. T. & Cislerova, M. Effect of the shape of the soil hydraulic functions near saturation on variably-saturated flow predictions. *Adv. Water Resour.* **24**, 133–144 (2000).

51. Long, D. et al. South-to-North water diversion stabilizing Beijing's groundwater levels. *Nat. Commun.* **11**, 3665 (2020).

52. Kendy, E. et al. A soil-water-balance approach to quantify groundwater recharge from irrigated cropland in the North China Plain. *Hydrol. Process.* **17**, 2011–2031 (2003).

53. Simons, G., Koster, R. & Droogers, P. *Hihydrosoil v2.0-high resolution soil maps of global hydraulic properties*. https://www.futurewater.eu/projects/hihydrosoil/ (2020).

54. Toth, B. et al. New generation of hydraulic pedotransfer functions for Europe. *Eur. J. Soil Sci.* **66**, 226–238 (2015).

55. Mualem, Y. A new model for predicting the hydraulic conductivity of unsaturated porous media. *Water Resour. Res.* **12**, 513–522 (1976).

56. Schaap, M. G. & van Genuchten, M. T. A modified Mualem-van Genuchten formulation for improved description of the hydraulic conductivity near saturation. *Vadose Zone J.* **5**, 27–34 (2006).

57. Peters, A., Durner, W. & Wessolek, G. Consistent parameter constraints for soil hydraulic functions. *Adv. Water Resour.* **34**, 1352–1365 (2011).

58. Shinomiya, Y., Takahashi, K., Kobiyama, M. & Kubota, J. Evaluation of the Tortuosity parameter for forest soils to predict unsaturated hydraulic conductivity. *J. For. Res. Jpn.* **6**, 221–225 (2001).

59. Lin, P., Pan, M., Wood, E. F., Yamazaki, D. & Allen, G. H. A new vector-based global river network dataset accounting for variable drainage density. *Sci. Data* **8**, 28 (2021).

60. Lehner, B., Verdin, K. & Jarvis, A. New Global Hydrography Derived From Spaceborne Elevation Data. *Eos, Trans. Am. Geophys. Union* **89**, 93–94 (2008).

61. Huscroft, J., Gleeson, T., Hartmann, J. & Borker, J. Compiling and mapping global permeability of the unconsolidated and consolidated earth: GLobal HYdrogeology MaPS 2.0 (GLHYMPS 2.0). *Geophys. Res. Lett.* **45**, 1897–1904 (2018).

62. Ran, Y. H. et al. New high-resolution estimates of the permafrost thermal state and hydrothermal conditions over the Northern Hemisphere. *Earth Syst. Sci. Data* **14**, 865–884 (2022).

63. Ge, S., Wu, Q. B., Lu, N., Jiang, G. L. & Ball, L. Groundwater in the Tibet Plateau, western China. *Geophys. Res. Lett.* **35**, L18403 (2008).

64. Yao, Y. Y. et al. Role of Groundwater in Sustaining Northern Himalayan Rivers. *Geophys. Res. Lett.* **48**, e2020GL092354 (2021).

65. Robson S. G. Techniques for estimating specific yield and specific retention from grain-size data and geophysical logs from clastic bedrock aquifers. In *Water-Resources Investigations Report 93-4198*. (US Department of the Interior, US Geological Survey, 1993).

66. Younger, P. L. Simple generalized methods for estimating aquifer storage parameters. *Q. J. Eng. Geol.* **26**, 127–135 (1993).

67. Ha, K., Ngoc, N. T. M., Lee, E. & Jayakumar, R. *Current status and issues of groundwater in the Mekong River basin*. (Korea Institute of Geoscience and Mineral Resources (KIGAM) Bangkok, Thailand, 2015).

68. Cuthbert, M. O. et al. Global patterns and dynamics of climate-groundwater interactions. *Nat. Clim. Change* **9**, 137–141 (2019).

69. de Graaf, I. E. M., Sutanudjaja, E. H., van Beek, L. P. H. & Bierkens, M. F. P. A high-resolution global-scale groundwater model. *Hydrol. Earth Syst. Sci.* **19**, 823–837 (2015).

70. de Graaf, I., Condon, L. & Maxwell, R. Hyper-Resolution Continental-Scale 3-D Aquifer Parameterization for Groundwater Modeling. *Water Resour. Res.* **56**, e2019WR026004 (2020).

71. IGRAC. Transboundary Aquifer Information Sheets. https://www.un-igrac.org/ggis/transboundary-aquifer-information-sheets (2015).

72. Kuang, X., Jiao, J., Zheng, C., Cherry, J. & Li, H. A review of specific storage in aquifers. *J. Hydrol.* **581**, 124383 (2020).

73. Wang, J. et al. Modeling daily floods in the lancang-mekong river basin using an improved hydrological-hydrodynamic model. *Water Resour. Res.* **57**, e2021WR029734 (2021).

74. He, X. et al. Solar and wind energy enhances drought resilience and groundwater sustainability. *Nat. Commun.* **10**, 4893 (2019).

75. Pokhrel, Y. et al. Global terrestrial water storage and drought severity under climate change. *Nat. Clim. Change* **11**, 226–233 (2021).

76. Li, Y. X. et al. Multi-model analysis of historical runoff changes in the Lancang-Mekong River Basin-Characteristics and uncertainties. *J. Hydrol.* **619**, 129297 (2023).

77. Mei, Y. et al. Can hydrological models benefit from using global soil moisture, evapotranspiration, and runoff products as calibration targets? *Water Resour. Res.* **59**, e2022WR032064 (2023).

78. Watkins, M. M., Wiese, D. N., Yuan, D. N., Boening, C. & Landerer, F. W. Improved methods for observing Earth's time variable mass distribution with GRACE using spherical cap mascons. *J. Geophys. Res. Solid Earth* **120**, 2648–2671 (2015).

79. Save, H., Bettadpur, S. & Tapley, B. D. High-resolution CSR GRACE RL05 mascons. *J. Geophys. Res. Solid Earth* **121**, 7547–7569 (2016).

80. Zou, Y. et al. Solid water melt dominates the increase of total groundwater storage in the Tibetan Plateau. *Geophys. Res. Lett.* **49**, e2022GL100092 (2022).

81. Condon, L. E., Atchley, A. L. & Maxwell, R. M. Evapotranspiration depletes groundwater under warming over the contiguous United States. *Nat. Commun.* **11**, 873 (2020).

82. Orth, O. S. R. Global soil moisture data derived through machine learning trained with in-situ measurements. *Sci. Data* **8**, 170 (2021).

83. Chen, X. & Hu, Q. Groundwater influences on soil moisture and surface evaporation. *J. Hydrol.* **297**, 285–300 (2004).

84. Maihemuti, B. et al. Development and evaluation of the soil water balance model in an inland arid delta oasis: Implications for sustainable groundwater resource management. *Glob. Ecol. Conserv* **25**, e01408 (2021).

85. Wang-Erlandsson, L. et al. A planetary boundary for green water. *Nat. Rev. Earth Environ.* **3**, 380–392 (2022).

86. Makkeh, A., Theis, D. O. & Vicente, R. Bivariate partial information decomposition: the optimization perspective. *Entropy* **19**, 530 (2017).

Acknowledgements

Author contributions

H.H. and J.L. conceived the research, and H.H. implemented modeling and data analysis. H.H. wrote the first paper draft together with L.G. and A.C., and D.C., I.G., and J.L. contributed to interpreting the results and discussion and improving the paper.

Competing interests

The authors declare no competing interests.

Additional information

Supplementary information The online version contains supplementary material available at https://doi.org/10.1038/s43247-025-02093-8.

Correspondence and requests for materials should be addressed to Junguo Liu.

Peer review information *Communications Earth & Environment* thanks the anonymous reviewers for their contribution to the peer review of this work. Primary Handling Editors: Rahim Barzegar and Alireza Bahadori. A peer review file is available.

Reprints and permissions information is available at http://www.nature.com/reprints

Publisher's note Springer Nature remains neutral with regard to jurisdictional claims in published maps and institutional affiliations.